# Thermal nature of the causal diamond horizon: A hidden property of the inertial propagator

Nada Eissa, <sup>1</sup> Carlos R. Ordóñez, <sup>1</sup> and Gustavo Valdivia-Mera <sup>1</sup>

<sup>1</sup>Department of Physics, University of Houston, Houston, Texas 77204-5005, USA

(Dated: August 26, 2025)

#### Abstract

Inspired by the novel idea proposed by T. Padmanabhan in Phys. Rev. D 100, 045024 (2019), we develop a method to uncover the hidden thermal properties of the inertial Feynman propagator in Minkowski spacetime in a causally consistent manner. This, in turn, enables a coherent interpretation based on future-directed propagation. In this method, the Fourier transform is implemented following the convention used in the analysis of vacuum fluctuations. As a result, future-directed propagation across causal horizons can be consistently interpreted, from the perspective of an observer confined to a causally disconnected region, as the emission of scalar quanta at the past horizon and their absorption at the future horizon. Furthermore, we find that the ratio of emission and absorption processes reproduces the characteristic Boltzmann factor of a thermal ensemble. We first apply this analysis to the right Rindler wedge, recovering the well-known Unruh temperature,  $T = a/(2\pi)$ . We then extend the analysis to a causal diamond of length  $2\alpha$ , performing a meticulous analysis of the near-horizon geometry and thereby obtaining the temperature associated with the thermal behavior of the Minkowski vacuum as perceived by an observer with finite lifetime  $2\alpha$ . Our results demonstrate that thermality can emerge directly from causal structure, independently of acceleration or gravity, with causal diamonds encoding intrinsic thermodynamic behavior in quantum field theory.

#### CONTENTS

I.	Introduction	3
II.	The Feynman propagator and causal diamond geometry	4
	A. The Feynman propagator and its frequency-space representation	4
	B. Causal diamond geometry	5
	1. Causal diamond spacetime from Rindler	5
	2. Complementary regions: wedges and diamonds	6
	3. Boundary of the causal diamond	8
III.	Thermal behavior of causal horizons: Insights from causally disconnected observers	10
	A. Method description	10
	B. Thermality of the Rindler horizons	11
	1. Two propagations in the $R$ wedge	12
	2. Propagation from the wedge $P$ to $R$ , and from $R$ to $F$	14
	C. Thermality of the causal diamond horizons	18
	1. Two propagations in the region $D_R$	19
	2. Propagation from the region $D_P$ to $D_R$ , and from $D_R$ to $D_F$	21
IV.	Discussion	25
	Acknowledgments	26
	References	26

#### I. INTRODUCTION

In his insightful work, T. Padmanabhan [1] showed that the inertial Feynman propagator for a real scalar field in Minkowski spacetime loses its time-reversal symmetry in the presence of causal horizons. Moreover, by considering the Fourier transform of the Feynman propagator with respect to the temporal interval, he interpreted backward-in-time propagation from the future wedge F to the right wedge R as the emission of scalar quanta from the horizon, while forward-in-time propagation from R to F was interpreted as absorption. Remarkably, the squared norm of the ratio of these Fourier-transformed propagators yields a thermal Boltzmann factor that reproduces the well-known Unruh temperature,  $T = a/(2\pi)$ , for uniformly accelerated observers [2–4].

In this article, we will adopt Padmanabhan's idea of using the Feynman propagator to characterize physical processes across causal horizons, as it naturally encodes the appropriate dependence on spacetime intervals. However, we treat the Fourier transform in the time interval in a distinct manner. Specifically, we introduce a physically motivated prescription for the Fourier transform, consistent with the conventions used in the analysis of vacuum fluctuations [5, 6]. Within this framework, in contrast to Padmanabhan's approach, we restrict our analysis to future-directed propagations between two events. Propagations that cross the causal horizon into the causally disconnected region are interpreted as the emission of scalar quanta, while those crossing out of the causally disconnected region correspond to their absorption. Furthermore, we implement a setup involving a triad of events that allows us to relate the emission and absorption processes.

This article is organized as follows: In Sec. II, we present the Feynman propagator in a representation that emphasizes its dependence on squared spacetime intervals and enables a useful Fourier transform in the time interval, followed by an analysis of the geometry of the causal diamond, focusing on its boundary structure in Minkowski spacetime and its near-horizon regime. In Sec. III, we describe the method that will be used in the remainder of the section, and then apply it to both the Rindler and causal diamond cases. We conclude in Sec. IV with a discussion of our results and their implications for the emergence of thermality from causal structure.

#### II. THE FEYNMAN PROPAGATOR AND CAUSAL DIAMOND GEOMETRY

#### A. The Feynman propagator and its frequency-space representation

The Feynman propagator in d-dimensional Minkowski spacetime for a real massive scalar field, with metric signature  $(-, +, +, \cdots)$ , can be expressed as

$$G_F(x-y) = i \left(\frac{1}{4\pi i}\right)^{d/2} \int_0^\infty \frac{ds}{s^{d/2}} \exp\left[\frac{i}{4s}\sigma^2(x,y) - ism^2 - s\epsilon\right],\tag{1}$$

where  $\epsilon \to 0^+$  enforces the appropriate boundary conditions for time ordering, and  $\sigma^2(x,y)$  denotes the squared Minkowski spacetime interval between the events  $x^{\mu}$  and  $y^{\mu}$  (for a detailed discussion on how to recover the standard form of the Feynman propagator as presented in Refs. [7, 8], see Ref. [9]). In addition, the dependence of the Feynman propagator  $G_F$  on the temporal coordinates arises solely through the interval  $\Delta t = x^0 - y^0$ , which is a direct consequence of the static nature of Minkowski spacetime.

In what follows, it will prove advantageous to work with a representation in which the time dependence of the propagator is transferred to its conjugate frequency domain. This is particularly useful when analyzing propagation across causal horizons or when exploiting the symmetries of static spacetimes. To this end, we introduce the *frequency-space propagator* by performing a Fourier transform of  $G_F$  with respect to the time interval, following the standard procedure for vacuum fluctuation detection [5, 6]:

$$\tilde{G}_F(\Omega, \mathbf{x}, \mathbf{y}) = \int_{-\infty}^{\infty} d(\Delta t) \, G_F(\Delta t, \mathbf{x}, \mathbf{y}) \, e^{-i\Omega \Delta t}, \tag{2}$$

where  $\Omega$  is the frequency conjugate to the time separation  $\Delta t$ . In Minkowski spacetime, the analytic structure of  $\tilde{G}_F(\Omega, \mathbf{x}, \mathbf{y})$  is characterized by simple poles at  $\Omega = \pm (\omega_{\mathbf{k}} - i\epsilon)$ . These singularities encode the causal and time-ordered nature of  $G_F$ . By restricting attention to  $\Omega > 0$ , we isolate the contribution of positive-frequency modes, which are naturally associated with physical excitations propagating forward in time.

#### B. Causal diamond geometry

#### 1. Causal diamond spacetime from Rindler

A causal diamond of length  $2\alpha$  in Minkowski spacetime is given by the region  $D_R$ , defined as  $D_R := \{(t,x) : |t| + |x| \le \alpha\}$ . This region corresponds to the causal domain of an observer with a finite lifetime, bounded by the intersection of the future light cone of the birth event at  $(t,x) = (-\alpha,0)$  and the past light cone of the death event at  $(t,x) = (\alpha,0)$ , as illustrated in Fig. 1a. Therefore, the boundary of the causal diamond precisely contains the causal horizon associated with this observer.

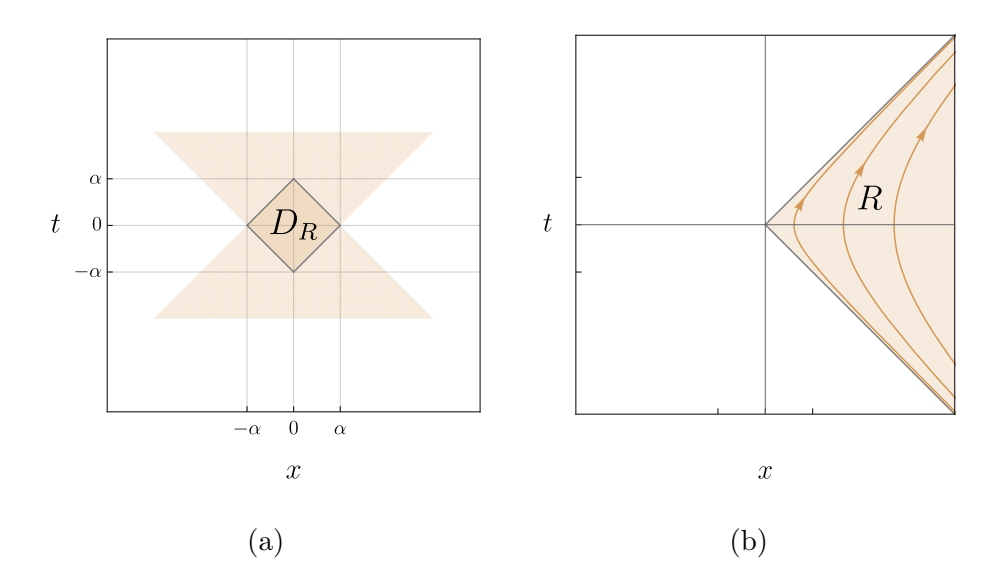


FIG. 1: (a) Causal diamond  $D_R$  defined as the intersection of a future and a past light cone. (b) Uniformly accelerated trajectories in the right Rindler wedge R.

The spacetime experienced by such a finite-lifetime observer defines the so-called Causal Diamond (CD) spacetime. It can be geometrically characterized from the subset of Minkowski spacetime points restricted to the region  $D_R$ , denoted as  $x^{\mu} = (t_{d_R}, x_{d_R})$ . These coordinates are obtained by applying the conformal transformation introduced in Ref. [10] to the Minkowski coordinates restricted to the right Rindler wedge R (see Fig. 1b), which are given by  $\tilde{x}^{\mu} = (t_r, x_r)$ . Accordingly, the conformal map is defined as

$$\tilde{x}^{\mu} \mapsto x^{\mu} = [T \circ K \circ D] \, \tilde{x}^{\mu}. \tag{3}$$

The transformation introduced in Eq. (3) is given by the following finite conformal group transformations (see [11]):

Dilation: 
$$D(\lambda)\tilde{x}^{\mu} = \lambda \,\tilde{x}^{\mu},$$
 (4)

Translation: 
$$T(c)\tilde{x}^{\mu} = \tilde{x}^{\mu} + c^{\mu},$$
 (5)

Special Conformal Transformation (SCT): 
$$K(b)\tilde{x}^{\mu} = \frac{\tilde{x}^{\mu} - b^{\mu}(\tilde{x} \cdot \tilde{x})}{1 - 2(b \cdot \tilde{x}) + (b \cdot b)(\tilde{x} \cdot \tilde{x})}.$$
 (6)

For later use, the parameters of the SCT and the translation are fixed as

$$b^{\mu} \equiv \left(0, -\frac{1}{2\alpha}\right) \quad , \quad c^{\mu} \equiv (0, -\alpha). \tag{7}$$

Now, consider the coordinates  $(t_r, x_r)$  defined through the following suitably rescaled transformation between Minkowski and Rindler coordinates  $(\eta, \rho)$  (for a more detailed discussion, see Ref. [10]):

$$\frac{t_r}{\tilde{\alpha}} = \left(\frac{2}{\alpha}\right) \rho \sinh\left(\frac{2\eta}{\alpha}\right) \quad , \quad \frac{x_r}{\tilde{\alpha}} = \left(\frac{2}{\alpha}\right) \rho \cosh\left(\frac{2\eta}{\alpha}\right), \tag{8}$$

where  $\tilde{\alpha} = 2\alpha/\lambda$ . Then, from Eqs. (3)–(7), we obtain the coordinate transformation between the Minkowski points restricted to the region  $D_R$  and the CD spacetime coordinates  $(\eta, \rho)$ :

$$t_{d_r} = \frac{4\alpha^2 \rho \sinh\left(\frac{2\eta}{\alpha}\right)}{\alpha^2 + 4\alpha\rho \cosh\left(\frac{2\eta}{\alpha}\right) + 4\rho^2} \quad , \quad x_{d_r} = \frac{4\alpha\rho^2 - \alpha^3}{\alpha^2 + 4\alpha\rho \cosh\left(\frac{2\eta}{\alpha}\right) + 4\rho^2}, \tag{9}$$

It is worth noting that the dilation parameter  $\lambda$  does not appear explicitly in Eq. (9), as it has been absorbed into the rescaled coordinate transformation between Minkowski and Rindler spacetimes introduced in Eq. (8).

The line element of the causal diamond (CD) spacetime takes the form

$$ds^2 = \Lambda^2(\eta, \rho) \left[ -\frac{4\rho^2}{\alpha^2} d\eta^2 + d\rho^2 \right], \tag{10}$$

where  $\eta \in (-\infty, \infty)$  and  $\rho > 0$ , with the conformal factor given by

$$\Lambda^{2}(\eta, \rho) = \frac{16\alpha^{4}}{\left(\alpha^{2} + 4\alpha\rho \cosh\left(\frac{2\eta}{\alpha}\right) + 4\rho^{2}\right)^{2}}.$$
(11)

#### 2. Complementary regions: wedges and diamonds

Minkowski spacetime contains not only the right Rindler wedge R, but also the left L, past P, and future F wedges, as shown in Fig. 2a. These additional regions, although regarded

as unphysical due to their unconventional causal structures, are nevertheless geometrically meaningful in the context of an extended conformal mapping. Accordingly, just as we characterized the region  $D_R$  from the wedge R via the conformal map in Eq. (3), we now construct the mappings from the wedges L, P, and F to their corresponding diamond regions  $D_L$ ,  $D_P$ , and  $D_F$ , respectively, as color-coded in Fig. 2b.

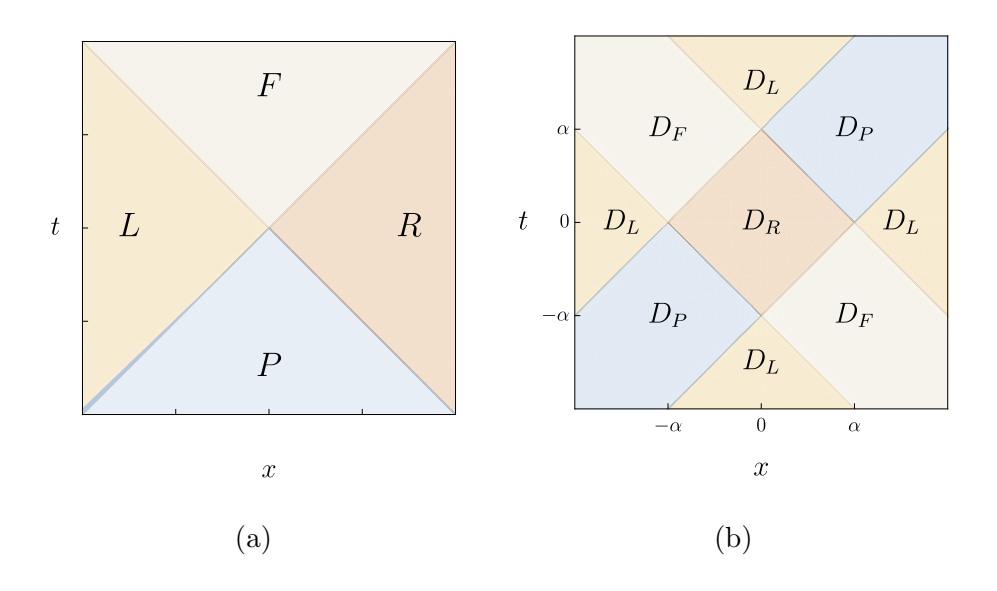


FIG. 2: (a) Rindler wedges, R, L, P, and F, in Minkowski spacetime. (b) Diamond regions  $D_R$ ,  $D_L$ ,  $D_P$ , and  $D_F$  in Minkowski spacetime.

To do so, we begin with the suitably rescaled transformations, analogous to those defined in Ref. [10], between the Minkowski and Rindler coordinates associated with the left, past, and future Rindler wedges:

$$\frac{t_l}{\tilde{\alpha}} = -\frac{2\rho}{\alpha} \sinh\left(\frac{2\eta}{\alpha}\right) \quad , \quad \frac{x_l}{\tilde{\alpha}} = -\frac{2\rho}{\alpha} \cosh\left(\frac{2\eta}{\alpha}\right), \tag{12}$$

$$\frac{t_l}{\tilde{\alpha}} = -\frac{2\rho}{\alpha} \sinh\left(\frac{2\eta}{\alpha}\right) , \quad \frac{x_l}{\tilde{\alpha}} = -\frac{2\rho}{\alpha} \cosh\left(\frac{2\eta}{\alpha}\right), \qquad (12)$$

$$\frac{t_f}{\tilde{\alpha}} = \frac{2\rho}{\alpha} \cosh\left(\frac{2\eta}{\alpha}\right) , \quad \frac{x_f}{\tilde{\alpha}} = \frac{2\rho}{\alpha} \sinh\left(\frac{2\eta}{\alpha}\right), \qquad (13)$$

$$\frac{t_p}{\tilde{\alpha}} = -\frac{2\rho}{\alpha} \cosh\left(\frac{2\eta}{\alpha}\right) \quad , \quad \frac{x_p}{\tilde{\alpha}} = -\frac{2\rho}{\alpha} \sinh\left(\frac{2\eta}{\alpha}\right). \tag{14}$$

Applying the conformal map (3), we obtain the Minkowski coordinates restricted to the regions  $D_L$ ,  $D_P$ , and  $D_F$ , denoted by  $(t, x) = (t_{d_i}, x_{d_i})$  with  $i \in \{l, p, f\}$ , expressed in terms of the causal diamond coordinates  $(\eta, \rho)$ :

$$t_{d_l} = \frac{-4\alpha^2 \rho \sinh\left(\frac{2\eta}{\alpha}\right)}{\alpha^2 - 4\alpha\rho \cosh\left(\frac{2\eta}{\alpha}\right) + 4\rho^2} , \quad x_{d_l} = \frac{4\alpha\rho^2 - \alpha^3}{\alpha^2 - 4\alpha\rho \cosh\left(\frac{2\eta}{\alpha}\right) + 4\rho^2},$$

$$t_{d_f} = \frac{4\alpha^2 \rho \cosh\left(\frac{2\eta}{\alpha}\right)}{\alpha^2 + 4\alpha\rho \sinh\left(\frac{2\eta}{\alpha}\right) - 4\rho^2} , \quad x_{d_f} = \frac{-4\alpha\rho^2 - \alpha^3}{\alpha^2 + 4\alpha\rho \sinh\left(\frac{2\eta}{\alpha}\right) - 4\rho^2},$$

$$t_{d_p} = \frac{-4\alpha^2 \rho \cosh\left(\frac{2\eta}{\alpha}\right)}{\alpha^2 - 4\alpha\rho \sinh\left(\frac{2\eta}{\alpha}\right) - 4\rho^2} , \quad x_{d_p} = \frac{-4\alpha\rho^2 - \alpha^3}{\alpha^2 - 4\alpha\rho \sinh\left(\frac{2\eta}{\alpha}\right) - 4\rho^2}.$$

$$(15)$$

$$t_{d_f} = \frac{4\alpha^2 \rho \cosh\left(\frac{2\eta}{\alpha}\right)}{\alpha^2 + 4\alpha\rho \sinh\left(\frac{2\eta}{\alpha}\right) - 4\rho^2} \quad , \quad x_{d_f} = \frac{-4\alpha\rho^2 - \alpha^3}{\alpha^2 + 4\alpha\rho \sinh\left(\frac{2\eta}{\alpha}\right) - 4\rho^2}, \tag{16}$$

$$t_{d_p} = \frac{-4\alpha^2 \rho \cosh\left(\frac{2\eta}{\alpha}\right)}{\alpha^2 - 4\alpha\rho \sinh\left(\frac{2\eta}{\alpha}\right) - 4\rho^2} \quad , \quad x_{d_p} = \frac{-4\alpha\rho^2 - \alpha^3}{\alpha^2 - 4\alpha\rho \sinh\left(\frac{2\eta}{\alpha}\right) - 4\rho^2}.$$
 (17)

#### Boundary of the causal diamond

Based on the coordinate transformations between points in Minkowski spacetime restricted to the regions  $D_R$ ,  $D_P$ , and  $D_F$ , and the causal diamond geometry associated to these regions, as given in Eqs. (9), (16)–(17), we observe a characteristic behavior of constant- $\rho$  trajectories within these regions. Specifically, for small values of  $\rho$ , the trajectories asymptotically approach the left boundary of the causal diamond  $D_R$ , while for large values of  $\rho$ , they approach the right boundary. These features are illustrated in Fig. 3.

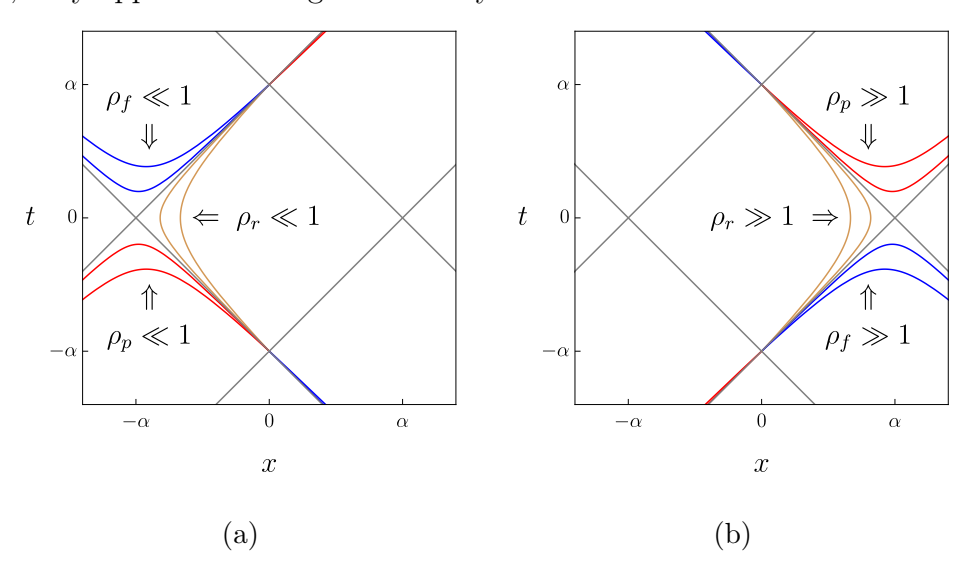


FIG. 3: Constant- $\rho$  trajectories for (a)  $\rho_{r,p,f} \ll 1$ , and (b)  $\rho_{r,p,f} \gg 1$ .

In order to characterize the boundary of the region  $D_R$ , let us begin by analyzing the expansion of  $(t_{d_R}, x_{d_R})$  in the regime  $\rho \ll 1$ , with  $\eta \in (-\infty, \infty)$ , which is given by:

$$t_{d_r} = 4\rho \sinh\left(\frac{2\eta}{\alpha}\right) - \frac{8\rho^2 \sinh\left(\frac{4\eta}{\alpha}\right)}{\alpha} + \frac{16\rho^3 \sinh\left(\frac{6\eta}{\alpha}\right)}{\alpha^2} + \mathcal{O}\left[(\rho/\alpha)^4\right],\tag{18}$$

$$x_{d_r} = -\alpha + 4\rho \cosh\left(\frac{2\eta}{\alpha}\right) - \frac{8\rho^2 \cosh\left(\frac{4\eta}{\alpha}\right)}{\alpha} + \frac{16\rho^3 \cosh\left(\frac{6\eta}{\alpha}\right)}{\alpha^2} + \mathcal{O}\left[(\rho/\alpha)^4\right]. \tag{19}$$

In addition, since  $\sinh(2\eta/\alpha) \approx \pm \cosh(2\eta/\alpha)$  for  $\eta \gg 1$  and  $\eta \ll -1$ , respectively, it follows from Eqs. (18) and (19) that, in the simultaneous limits  $\rho \to 0$  and  $\eta \to \pm \infty$ , one obtains the following causal horizons:

$$\mathcal{H}_0^+: \quad t_{d_r} = x_{d_r} + \alpha \,, \qquad \rho \to 0, \ \eta \to +\infty,$$
 (20)

$$\mathcal{H}_0^-: \quad t_{d_r} = -x_{d_r} - \alpha \,, \qquad \rho \to 0, \ \eta \to -\infty,$$
 (21)

where  $-\alpha < x_{d_r} < 0$ . These horizons are depicted on the left boundary (blue) of the region  $D_R$  in Fig. 4. On the other hand, we now turn to the expansion of  $(t_{d_r}, x_{d_r})$  in the regime  $\rho \gg 1$ , with  $\eta \in (-\infty, \infty)$ , from which we obtain:

$$t_{d_r} = \frac{\alpha^2 \sinh\left(\frac{2\eta}{\alpha}\right)}{\rho} - \frac{\alpha^3 \sinh\left(\frac{4\eta}{\alpha}\right)}{2\rho^2} + \frac{\alpha^4 \sinh\left(\frac{6\eta}{\alpha}\right)}{4\rho^3} + \mathcal{O}\left[\left(\rho/\alpha\right)^{-4}\right],\tag{22}$$

$$x_{d_r} = \alpha - \frac{\alpha^2 \cosh\left(\frac{2\eta}{\alpha}\right)}{\rho} + \frac{\alpha^3 \cosh\left(\frac{4\eta}{\alpha}\right)}{2\rho^2} - \frac{\alpha^4 \cosh\left(\frac{6\eta}{\alpha}\right)}{4\rho^3} + \mathcal{O}\left[\left(\rho/\alpha\right)^{-4}\right]. \tag{23}$$

As in the previous case, applying the limits  $\rho \to \infty$  and  $\eta \to \pm \infty$  to Eqs. (22) and (23) yields the following causal horizons:

$$\mathcal{H}_{\infty}^{+}: \quad t_{d_r} = -x_{d_r} + \alpha \quad , \quad \rho \to \infty \; , \; \eta \to \infty,$$
 (24)

$$\mathcal{H}_{\infty}^{-}: \quad t_{d_r} = x_{d_r} - \alpha \quad , \quad \rho \to \infty \; , \; \eta \to -\infty,$$
 (25)

where  $0 < x_{d_r} < \alpha$ . These horizons are depicted on the right boundary (red) of the region  $D_R$  in Fig. 4.

Finally, the asymptotic regions of the causal diamond spacetime, corresponding to the four corners of  $D_R$ , can be identified by analyzing the coordinate transformations between Minkowski and causal diamond spacetimes in the appropriate limits:

$$i^0: (t_{d_R}, x_{d_R}) = (0, -\alpha) , \quad \rho \to 0, \ \eta \in (-\infty, \infty),$$
 (26)

$$i^{\infty}: (t_{d_R}, x_{d_R}) = (0, \alpha) \quad , \quad \rho \to \infty, \ \eta \in (-\infty, \infty),$$
 (27)

$$i^-: (t_{d_R}, x_{d_R}) = (-\alpha, 0) , \quad \rho \in (0, \infty), \quad \eta \to -\infty,$$
 (28)

$$i^{+}: (t_{d_{R}}, x_{d_{R}}) = (\alpha, 0) , \quad \rho \in (0, \infty), \quad \eta \to \infty.$$
 (29)

In Fig. 4, we have included all the elements that characterize the causal structure of the boundary of the diamond  $D_R$ .

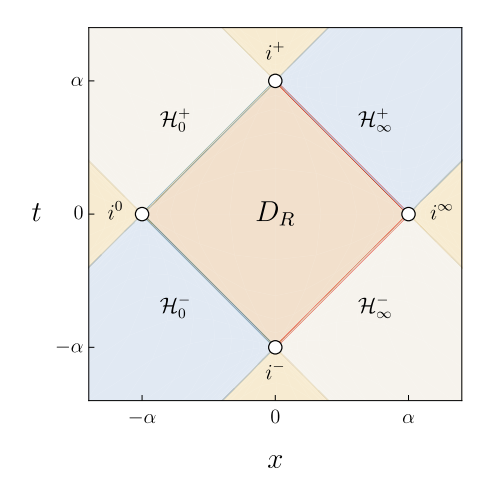


FIG. 4: Causal characterization of the boundary of the diamond  $D_R$ .

## III. THERMAL BEHAVIOR OF CAUSAL HORIZONS: INSIGHTS FROM CAUSALLY DISCONNECTED OBSERVERS

#### A. Method description

The method implemented in the following subsections can be summarized in the application of the following steps:

- 1. The calculation of the Feynman propagator  $G_F$  between events within causally disconnected regions of Minkowski spacetime, given by the right Rindler wedge R and the causal diamond  $D_R$ , as well as between events whose spacetime interval crosses the past and future horizons of these regions.
- 2. The application of the Fourier transform to the Feynman propagator in the interval  $\Delta \eta$ , which produces the frequency-space propagator  $\tilde{G}_F$ . This computation requires additional careful analysis for events whose spacetime interval crosses the causal horizons, due to the ill-defined notion of time associated with the  $\eta$  coordinate in the regions P, F,  $D_P$ , and  $D_F$ .
- 3. Implementation of the following setup: we consider two spacetime intervals in Minkowski, where  $x^{\mu}$  is the common event between both intervals,  $y^{\mu}$  lies in the past of  $x^{\mu}$ , while  $\bar{y}^{\mu}$  lies in its future. Furthermore,  $y^{\mu}$  and  $\bar{y}^{\mu}$  are related by a reflection in the Minkowski time coordinate. This setup finally allows us to compute the ratio between the frequency-space propagators  $\tilde{G}_F$  associated with the mentioned spacetime intervals.

#### B. Thermality of the Rindler horizons

In this section, we analyze propagation from the perspective of an observer undergoing constant acceleration in Minkowski spacetime, whose trajectory is confined to a specific region of the manifold — namely, the right Rindler wedge R, as shown in Fig. 1b. A key feature of this non-inertial observer is their notion of temporal evolution, governed by the Killing vector field  $\partial_{\eta}$ , whose geometric flow can be represented in Minkowski spacetime through the coordinate map in Eq. (8). This flow corresponds — up to a constant scaling factor — to the Lorentz boost generator in Minkowski spacetime, as illustrated in Fig. 5. Moreover, the same geometric flow provides the coordinate maps in the remaining wedges L, F, and P, which are explicitly given in Eqs. (12)–(14).

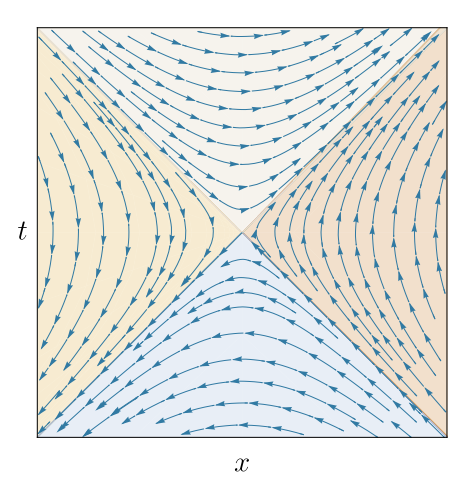


FIG. 5: Geometric flow associated with the Killing vector field  $\partial_{\eta}$ : timelike in wedges R and L, spacelike in wedges P and F, and null on the horizons  $t = \pm x$ .

It is important to note that the behavior of  $\partial_{\eta}$  in the extended Minkowski geometry is such that its character changes upon crossing the causal horizons  $t = \pm x$ , which directly affects the meaning of  $\eta$  as a time coordinate and, consequently, the coordinate mapping with respect to Minkowski. More precisely, in the wedge R the notion of time given by the vector field  $\partial_{\eta}$ , which is timelike, is well defined and future-directed with respect to Minkowski time. On the causal horizons  $\partial_{\eta}$  becomes null (or lightlike). Then, in the wedge L, the vector field  $\partial_{\eta}$  is timelike again but past-directed relative to R. In contrast, in the wedges P and F, the vector field  $\partial_{\eta}$  becomes spacelike, implying that  $\eta$  no longer serves as a physical time coordinate in those wedges.

Taking into account the details just discussed, in what follows we will analyze the behavior of the Feynman propagator  $G_F$  between events whose spacetime interval is confined to the Rindler wedge R, as well as the case in which the interval crosses the past and future Rindler horizons — namely, propagation from the wedge P into R, and from R into F. Additionally, the computation of the frequency-space propagator  $\tilde{G}_F$  will reveal how the nature of the causal horizon — which precisely denotes the change in the character of  $\partial_{\eta}$  and, consequently, the coordinate mapping — affects the ratio between two propagations that are physically equivalent from the perspective of an inertial observer.

#### 1. Two propagations in the R wedge

Let us consider the configurations shown in Figs. 6a and 6b, where Path 1 corresponds to the propagation from the event  $y^{\mu} \equiv (y^0, y^1)$  to  $x^{\mu} \equiv (x^0, x^1)$ , while Path 2 corresponds to the propagation from  $\bar{x}^{\mu} \equiv (\bar{x}^0, \bar{x}^1)$  to  $\bar{y}^{\mu} \equiv (\bar{y}^0, \bar{y}^1)$ . Notice that both propagations take place within the right Rindler wedge R. To describe the Feynman propagator from the viewpoint of the Rindler observer, we apply the coordinate transformation between Minkowski coordinates — restricted to the right wedge — and Rindler coordinates  $(\eta, \rho)$ , given by the standard form (as in Eq. (8), with  $2/\alpha = a$  and  $\tilde{\alpha}a = 1$ ):

$$x^{0} = \rho_{x} \sinh (a\eta_{x}) \quad , \quad x^{1} = \rho_{x} \cosh (a\eta_{x}), \tag{30}$$

$$y^{0} = \rho_{y} \sinh (a\eta_{y}) \quad , \quad y^{1} = \rho_{y} \cosh (a\eta_{y}), \tag{31}$$

$$\bar{x}^0 = \bar{\rho}_x \sinh(a\bar{\eta}_x)$$
 ,  $\bar{x}^1 = \bar{\rho}_x \cosh(a\bar{\eta}_x)$ , (32)

$$\bar{y}^0 = \bar{\rho}_y \sinh(a\bar{\eta}_y)$$
 ,  $\bar{y}^1 = \bar{\rho}_y \cosh(a\bar{\eta}_y)$ . (33)

Thus, we obtain the following squared spacetime intervals:

Path 1: 
$$\sigma^2(x,y) = -(x^0 - y^0)^2 + (x^1 - y^1)^2$$
  

$$= \rho_x^2 + \rho_y^2 - 2\rho_x\rho_y \cosh\left[a(\eta_x - \eta_y)\right],$$
Path 2:  $\sigma^2(\bar{x}, \bar{y}) = -(\bar{y}^0 - \bar{x}^0)^2 + (\bar{y}^1 - \bar{x}^1)^2$ 
(34)

$$= \bar{\rho}_x^2 + \bar{\rho}_y^2 - 2\bar{\rho}_x\bar{\rho}_y \cosh\left[a(\bar{\eta}_x - \bar{\eta}_y)\right]. \tag{35}$$

We note the following: (1) Clearly, the forms of the squared spacetime intervals for Paths 1 and 2 are identical, up to a relabeling. This is because both propagations occur within

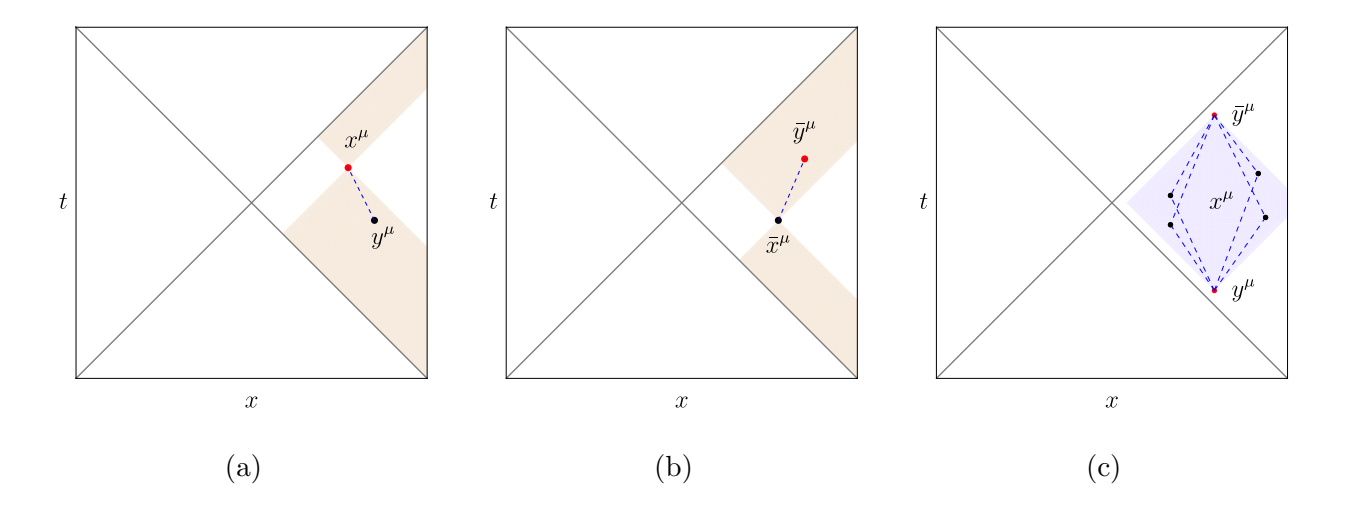


FIG. 6: (a) Path 1: From  $y^{\mu} \in R$  to  $x^{\mu} \in R$ . (b) Path 2: From  $\bar{x}^{\mu} \in R$  to  $\bar{y}^{\mu} \in R$ . (c) Paths 1 and 2, where  $x^{\mu} = \bar{x}^{\mu}$  and  $y^{\mu}$  is related to  $\bar{y}^{\mu}$  by a time reflection.

the same wedge, thus employing the same mapping between the Rindler and Minkowski coordinates; (2) the time dependence arises exclusively through the intervals  $\Delta \eta = \eta_x - \eta_y$  and  $\Delta \bar{\eta} = \bar{\eta}_x - \bar{\eta}_y$ , which is a direct consequence of the static nature of the Rindler spacetime geometry. This enables the computation of the frequency-space propagators  $\tilde{G}_F(\Omega, \rho_x, \rho_y)$  and  $\tilde{G}_F(\bar{\Omega}, \bar{\rho}_x, \bar{\rho}_y)$ , defined via Fourier transforms with respect to  $\Delta \eta$  and  $\Delta \bar{\eta}$ , respectively, as introduced in Eq. (2); (3) the squared spacetime intervals for Paths 1 and 2 are invariant under the transformations  $\Delta \eta \to -\Delta \eta$  and  $\Delta \bar{\eta} \to -\Delta \bar{\eta}$ , respectively. This represents a feature inherited from the inertial propagator, resulting from the fact that the coordinate map relates static geometries (Minkowski and Rindler).

To compare the two propagators, we now consider the following setup:  $x^{\mu} = \bar{x}^{\mu}$  and  $\bar{y}^{\mu} \equiv (-y^0, y^1)$ , as illustrated in Fig. 6c. This implies  $\bar{\eta}_x = \eta_x$ ,  $\bar{\rho}_x = \rho_x$ ,  $\bar{\eta}_y = -\eta_y$ , and  $\bar{\rho}_y = \rho_y$ . Hence, we have  $\Delta \eta = \eta_x - \eta_y$  and  $\Delta \bar{\eta} = \eta_x + \eta_y$ . Substituting these expressions into Eqs. (34) and (35), we obtain:

Path 1: 
$$\sigma^2(x,y) = \rho_x^2 + \rho_y^2 - 2\rho_x \rho_y \cosh[a(\eta_x - \eta_y)],$$
 (36)

Path 2: 
$$\sigma^2(x, \bar{y}) = \rho_x^2 + \rho_y^2 - 2\rho_x \rho_y \cosh[a(\eta_x + \eta_y)].$$
 (37)

The frequency-space propagator associated with Path 1 is then:

$$\tilde{G}_{F}^{\text{Path 1}}(\Omega, \rho_{x}, \rho_{y}) = \int_{-\infty}^{\infty} d(\Delta \eta) G_{F}^{\text{Path 1}}(\Delta \eta, \rho_{x}, \rho_{y}) e^{-i\Omega \Delta \eta},$$

$$= \int_{0}^{\infty} \frac{ds}{4\pi s} \exp\left[\frac{i}{4s}(\rho_{x}^{2} + \rho_{y}^{2}) - ism^{2} - s\epsilon\right]$$

$$\times \int_{-\infty}^{\infty} d(\Delta \eta) \exp\left[-\frac{i}{2s}\rho_{x}\rho_{y}\cosh(a\Delta \eta)\right] e^{-i\Omega \Delta \eta}$$

$$= \int_{0}^{\infty} \frac{ds}{4\pi s} \exp\left[\frac{i}{4s}(\rho_{x}^{2} + \rho_{y}^{2}) - ism^{2} - s\epsilon\right] \left[\frac{2}{a}K_{i\Omega/a}\left(\frac{i\rho_{x}\rho_{y}}{2s}\right)\right]. \tag{38}$$

Here we have used Eq.  $7^7$  in Sec. 8.432 of Ref. [12],

$$K_{\nu}(\zeta z) = \frac{z^{\nu}}{2} \int_0^{\infty} \exp\left[-\zeta \frac{\gamma + z^2 \gamma^{-1}}{2}\right] \gamma^{-\nu - 1} d\gamma, \quad |\arg(z)| \le \frac{\pi}{4}, \quad \operatorname{Re}(\nu) < 1, \tag{39}$$

with the identifications  $\zeta = i\rho_x \rho_y/(2s)$ ,  $\gamma = e^{a\Delta\eta}$ , z = 1, and  $\nu = i\Omega/a$ .

Similarly, for Path 2 we have:

$$\tilde{G}_F^{\text{Path 2}}(\bar{\Omega}, \rho_x, \rho_y) = \int_{-\infty}^{\infty} d(\Delta \bar{\eta}) G_F^{\text{Path 2}}(\Delta \bar{\eta}, \rho_x, \rho_y) e^{-i\bar{\Omega}\Delta \bar{\eta}}.$$
(40)

Since  $\Delta \eta$  and  $\Delta \bar{\eta}$  are dummy integration variables, it is clear that by setting  $\bar{\Omega} = \Omega$  the two expressions become identical. Thus, we find

$$\tilde{G}_F^{\text{Path 1}}(\Omega, \rho_x, \rho_y) = \tilde{G}_F^{\text{Path 2}}(\Omega, \rho_x, \rho_y). \tag{41}$$

This result demonstrates that propagation between events within the Rindler wedge R, where the time evolution generated by  $\partial_{\eta}$  is well-defined and consequently so is the time interval  $\Delta \eta$ , are physically equivalent for both Paths 1 and 2. This is fully consistent with the perspective of an inertial observer in Minkowski spacetime.

#### 2. Propagation from the wedge P to R, and from R to F

Let us consider the configurations shown in Figs. 7a and 7b, where Path 1 corresponds to the propagation from the event  $y^{\mu} \equiv (y^0, y^1) \in P$  to  $x^{\mu} \equiv (x^0, x^1) \in R$ , and Path 2 corresponds to the propagation from the event  $\bar{x}^{\mu} \equiv (\bar{x}^0, \bar{x}^1) \in R$  to  $\bar{y}^{\mu} \equiv (\bar{y}^0, \bar{y}^1) \in F$ . Importantly, the left wedge L is excluded from this analysis, since there is no causal connection — according to an inertial observer in Minkowski spacetime — between points located in

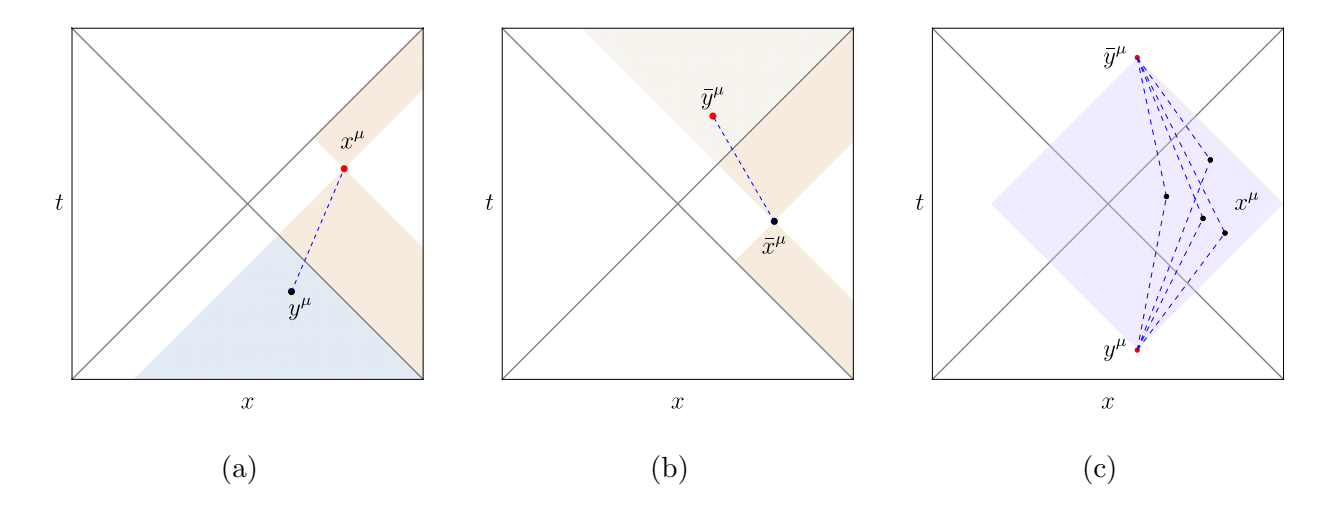


FIG. 7: (a) Path 1: From  $y^{\mu} \in P$  to  $x^{\mu} \in R$ . (b) Path 2: From  $\bar{x}^{\mu} \in R$  to  $\bar{y}^{\mu} \in F$ . (c) Paths 1 and 2, where  $x^{\mu} = \bar{x}^{\mu}$  and  $y^{\mu}$  is related to  $\bar{y}^{\mu}$  by a time reflection.

wedges R and L. In what follows, we present the coordinate transformations between the Minkowski coordinates restricted to each wedge involved in this analysis and their respective Rindler charts, given by the standard forms of Eqs. (8) and (13)–(14):

$$y^{0} = -\rho_{p} \cosh \left(a\eta_{p}\right) \quad , \quad y^{1} = -\rho_{p} \sinh \left(a\eta_{p}\right), \tag{42}$$

$$x^{0} = \rho_{r} \sinh (a\eta_{r}) \quad , \quad x^{1} = \rho_{r} \cosh (a\eta_{r}), \tag{43}$$

$$\bar{x}^0 = \bar{\rho}_r \sinh(a\bar{\eta}_r) \quad , \quad \bar{x}^1 = \bar{\rho}_r \cosh(a\bar{\eta}_r),$$
 (44)

$$\bar{y}^0 = \bar{\rho}_f \cosh\left(a\bar{\eta}_f\right) \quad , \quad \bar{y}^1 = \bar{\rho}_f \sinh\left(a\bar{\eta}_f\right).$$
 (45)

Thus, we obtain the following squared spacetime intervals:

Path 1: 
$$\sigma^2(x,y) = -(x^0 - y^0)^2 + (x^1 - y^1)^2$$
  

$$= -\rho_p^2 + \rho_r^2 - 2\rho_p \rho_r \sinh\left[a(\eta_r - \eta_p)\right], \tag{46}$$

Path 2: 
$$\sigma^2(\bar{x}, \bar{y}) = -(\bar{y}^0 - \bar{x}^0)^2 + (\bar{y}^1 - \bar{x}^1)^2$$
  

$$= -\bar{\rho}_f^2 + \bar{\rho}_r^2 + 2\bar{\rho}_f\bar{\rho}_r \sinh\left[a(\bar{\eta}_r - \bar{\eta}_f)\right]. \tag{47}$$

As we can see, the propagations for Paths 1 and 2 occur between regions with different coordinate charts, where the notions of time and space are effectively interchanged. As a result, the squared spacetime intervals for these paths are manifestly different, and they also differ from the case in which both Path 1 and Path 2 lie within the same wedge R, as given in Eqs. (34) and (35), where the temporal-interval-dependent function was expressed

in terms of the hyperbolic cosine. Nevertheless, the time dependence continues to appear through the intervals  $\Delta \eta = \eta_r - \eta_p$  and  $\Delta \bar{\eta} = \bar{\eta}_r - \bar{\eta}_f$ , since in the wedges relevant to this analysis the metric remains independent of  $\eta$ . Moreover, in the present case, the squared spacetime intervals for Paths 1 and 2 are no longer invariant under the transformations  $\Delta \eta \to -\Delta \eta$  and  $\Delta \bar{\eta} \to -\Delta \bar{\eta}$ , respectively. This clearly indicates not only that the two propagations are physically distinct, but also reflects the interchange of time and space in the coordinate maps employed. In addition, because the notion of  $\eta$  as a time coordinate is ill-defined in the P and F wedges, these intervals are to be understood in such a way that  $\eta_p$  and  $\bar{\eta}_f$ — not being physically meaningful time coordinates — merely correspond to shifts of the Rindler time coordinate in region R. Consequently, the Fourier transforms of  $G_F$  with respect to  $\Delta \eta$  and  $\Delta \bar{\eta}$  are effectively carried out in terms of  $\eta_r$  and  $\bar{\eta}_r$ , respectively. To compare both propagators, we identify  $\bar{x}^\mu = x^\mu$  and  $\bar{y}^\mu \equiv (-y^0, y^1)$ , as illustrated in Fig. 7c. Consequently, we have  $\bar{\eta}_r = \eta_r$ ,  $\bar{\rho}_r = \rho_r$ ,  $\bar{\eta}_f = -\eta_p$ , and  $\bar{\rho}_f = \rho_p$ , so that  $\Delta \eta = \eta_r - \eta_p$  and  $\Delta \bar{\eta} = \eta_r + \eta_p$ . Thus, the squared spacetime intervals in Eqs. (46) and (47) then become:

Path 1: 
$$\sigma^2(x,y) = -\rho_p^2 + \rho_r^2 - 2\rho_p\rho_r \sinh[a(\eta_r - \eta_p)],$$
 (48)

Path 2: 
$$\sigma^2(x, \bar{y}) = -\rho_n^2 + \rho_r^2 + 2\rho_p \rho_r \sinh[a(\eta_r + \eta_p)].$$
 (49)

Accordingly, the frequency-space propagator for Path 1 is given by

$$\begin{split} \tilde{G}_F^{\text{Path 1}}(\Omega,\rho_p,\rho_r) &= \int_{-\infty}^{\infty} d\eta_r \, G_F^{\text{Path 1}}(\eta_r - \eta_p,\rho_p,\rho_r) e^{-i\Omega\eta_r} \\ &= \int_{-\infty}^{\infty} d(\Delta\eta) \, G_F^{\text{Path 1}}(\Delta\eta,\rho_p,\rho_r) e^{-i\Omega\Delta\eta} e^{-i\Omega\eta_p} \\ &= \int_{0}^{\infty} \frac{ds}{4\pi s} \exp\left[\frac{i}{4s}(-\rho_p^2 + \rho_r^2) - ism^2 - s\epsilon\right] \\ &\qquad \times \int_{-\infty}^{\infty} d(\Delta\eta) \, e^{[-i/(2s)]\rho_p\rho_r \sinh(a\Delta\eta)} e^{-i\Omega\Delta\eta} e^{-i\Omega\eta_p} \\ &= \int_{0}^{\infty} \frac{ds}{4\pi s} \exp\left[\frac{i}{4s}(-\rho_p^2 + \rho_r^2) - ism^2 - s\epsilon\right] \left[\frac{2e^{-i\Omega\eta_p} e^{-\frac{\pi\Omega}{2a}}}{a} K_{-i\Omega/a} \left(-\frac{\rho_p\rho_r}{2s}\right)\right], (50) \end{split}$$

where we used the identity

$$2e^{-\operatorname{sign}(\zeta)\pi\nu/2}K_{i\nu}(2\zeta) = \int_0^\infty \exp\left[i\zeta(\gamma - \gamma^{-1})\right]\gamma^{i\nu-1}d\gamma, \quad \zeta \in \mathbb{R}, \ -1 < \operatorname{Im}(\nu) < 1, \quad (51)$$

with the substitutions  $\zeta = -\rho_p \rho_r/(4s)$ ,  $\gamma = e^{a\Delta\eta}$ , and  $\nu = -\Omega/a$ .

As seen from Eq. (50), and noting that the Macdonald function  $K_{i\nu}(2\zeta)$  is even in its order, we obtain the identity:

$$\tilde{G}_F^{\text{Path 1}}(-\Omega, \rho_p, \rho_r) = e^{\pi\Omega/a} \, \tilde{G}_F^{\text{Path 1}}(\Omega, \rho_p, \rho_r). \tag{52}$$

Similarly, for Path 2 we obtain:

$$\tilde{G}_{F}^{\text{Path 2}}(\bar{\Omega}, \rho_{p}, \rho_{r}) = \int_{-\infty}^{\infty} d\eta_{r} G_{F}^{\text{Path 2}}(\eta_{r} + \eta_{p}, \rho_{p}, \rho_{r}) e^{-i\bar{\Omega}\eta_{r}} 
= \int_{-\infty}^{\infty} d(\Delta\bar{\eta}) G_{F}^{\text{Path 2}}(\Delta\bar{\eta}, \rho_{p}, \rho_{r}) e^{-i\bar{\Omega}\Delta\bar{\eta}} e^{i\bar{\Omega}\eta_{p}} 
= \int_{0}^{\infty} \frac{ds}{4\pi s} \exp\left[\frac{i}{4s}(-\rho_{p}^{2} + \rho_{r}^{2}) - ism^{2} - s\epsilon\right] 
\times \int_{-\infty}^{\infty} d(\Delta\bar{\eta}) e^{[i/(2s)]\rho_{p}\rho_{r} \sinh(a\Delta\bar{\eta})} e^{-i\bar{\Omega}\Delta\bar{\eta}} e^{i\bar{\Omega}\eta_{p}} 
= \int_{0}^{\infty} \frac{ds}{4\pi s} \exp\left[\frac{i}{4s}(-\rho_{p}^{2} + \rho_{r}^{2}) - ism^{2} - s\epsilon\right] \left[\frac{2e^{i\bar{\Omega}\eta_{p}} e^{\frac{\pi\bar{\Omega}}{2a}}}{a} K_{i\bar{\Omega}/a}\left(-\frac{\rho_{p}\rho_{r}}{2s}\right)\right], (53)$$

where we have used the change  $\Delta \bar{\eta} \to -\Delta \bar{\eta}$  and applied Eq. (51) with  $\zeta = -\rho_p \rho_r/(4s)$ ,  $\gamma = e^{a\Delta \bar{\eta}}$ , and  $\nu = \Omega/a$ . Setting  $\bar{\Omega} = \Omega$ , we finally obtain:

$$\tilde{G}_F^{\text{Path 2}}(\Omega, \rho_p, \rho_r) = \tilde{G}_F^{\text{Path 1}}(-\Omega, \rho_p, \rho_r). \tag{54}$$

Therefore, from Eq. (52), the squared modulus of the ratio between the two frequency-space propagators is

$$\left| \frac{\tilde{G}_F^{\text{Path 1}}(\Omega, \rho_p, \rho_r)}{\tilde{G}_F^{\text{Path 2}}(\Omega, \rho_p, \rho_r)} \right|^2 = e^{-\beta\Omega} \quad , \quad \beta = 2\pi/a.$$
 (55)

This ratio is governed by a Boltzmann factor with an effective temperature equal to the Unruh temperature,  $T = a/(2\pi)$ . Therefore, from the perspective of the observer confined to wedge R, Path 1 — describing propagation from the P wedge into R — represents the emission of scalar quanta from the past horizon, whereas Path 2 — describing propagation from R into F — represents their absorption at the future horizon. This result highlights that, although from the perspective of an inertial observer propagations across causal horizons are physically equivalent, for the Rindler observer these processes become a clear manifestation of the thermality associated with the causal horizons — an effect that remains hidden in the inertial propagator.

#### C. Thermality of the causal diamond horizons

In this section, we analyze the propagation process from the perspective of an observer with finite lifetime  $2\alpha$ , confined to the region  $D_R$ , as illustrated in Fig. 1a. The causal diamond spacetime metric, given by the line element in Eq. (10), explicitly depends on the temporal coordinate  $\eta$ , which precludes the existence of a Killing vector field associated with it. Nevertheless, the generator of temporal evolution,  $\partial_{\eta}$ , is a conformal Killing vector (the relevance of this vector field within the causal diamond geometry has been explored in Refs. [13–16]). The flow generated by  $\partial_{\eta}$  in the extended Minkowski geometry, shown in Fig. 8, determines the coordinate transformations for the regions  $D_L$ ,  $D_P$ , and  $D_F$ , as given in Eqs. (15)–(17). Notably,  $\partial_{\eta}$  is timelike in  $D_R$  and  $D_L$ , with the temporal direction in  $D_R$  aligned with Minkowski time, while it is reversed in  $D_L$ . This vector field becomes null on the causal horizons and is spacelike in the regions  $D_P$  and  $D_F$ . Hence, the causal horizons precisely delimit the nature of  $\partial_{\eta}$  and, consequently, the coordinate mapping in each region.

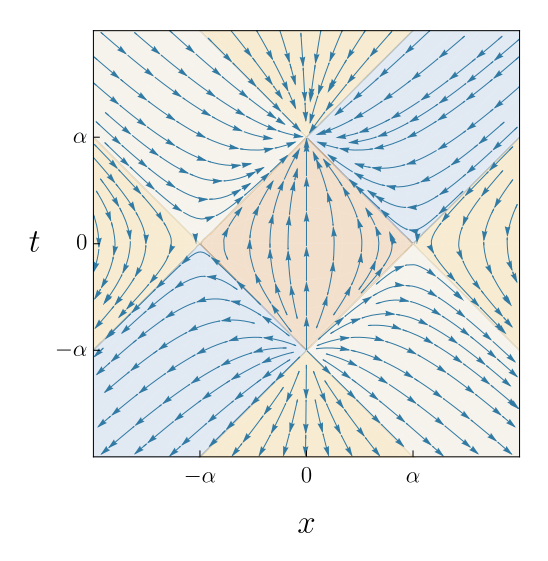


FIG. 8: Geometric flow associated with the Killing vector field  $\partial_{\eta}$ , which is timelike within the regions  $D_R$  and  $D_L$ , and spacelike in the regions  $D_F$  and  $D_P$ .

It is important to emphasize that, due to the explicit  $\eta$ -dependence of the causal diamond metric (this spacetime is not static), the full calculation of the frequency-space propagator  $\tilde{G}_F$  for propagations within the region  $D_R$ , as well as for those crossing the past and future causal horizons, becomes significantly non-trivial. Nevertheless, applying a near-horizon

analysis in the diamond region, we find that in the asymptotic regimes  $\rho \ll 1$  and  $\rho \gg 1$ , the effective metric is static to first order in  $\rho$  and  $1/\rho$ , respectively. Therefore, to simplify the analysis and properly define  $\tilde{G}_F$ , we restrict our attention to the regions near the horizons. This approach is natural, as the method does not impose any restriction on how close or far one must be from the horizon. In fact, for propagations that cross the causal horizons, what matters most is the crossing itself.

#### Two propagations in the region $D_R$

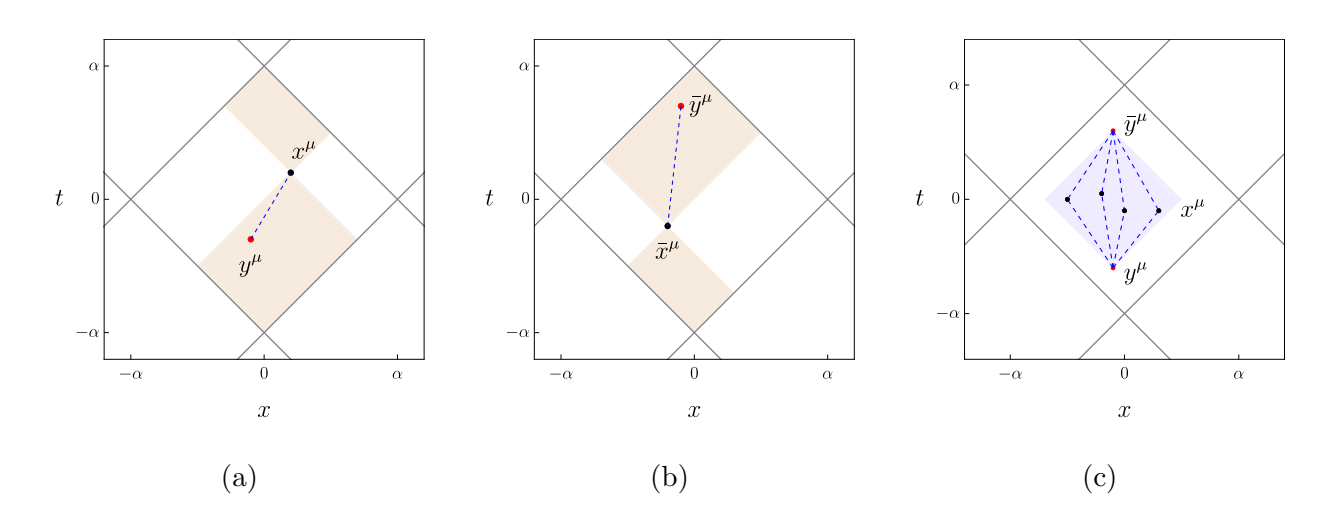


FIG. 9: (a) Path 1: From  $y^{\mu} \in D_R$  to  $x^{\mu} \in D_R$ . (b) Path 2: From  $\bar{x}^{\mu} \in D_R$  to  $\bar{y}^{\mu} \in D_R$ . (c) Paths 1 and 2, where  $x^{\mu} = \bar{x}^{\mu}$  and  $y^{\mu}$  is related to  $\bar{y}^{\mu}$  by a time reflection.

Let us consider the configurations shown in Figs. 9a and 9b, where Path 1 corresponds to the propagation from the event  $y^{\mu} \equiv (y^0, y^1)$  to  $x^{\mu} \equiv (x^0, x^1)$ , while Path 2 corresponds to the propagation from  $\bar{x}^{\mu} \equiv (\bar{x}^0, \bar{x}^1)$  to  $\bar{y}^{\mu} \equiv (\bar{y}^0, \bar{y}^1)$ , both propagations localized within the region  $D_R$ . To evaluate the situation from the perspective of the causal diamond observer, we employ the coordinate transformation given in Eq. (9):

$$x^{0} = \frac{4\alpha^{2}\rho_{x}\sinh\left(\frac{2\eta_{x}}{\alpha}\right)}{\alpha^{2} + 4\alpha\rho_{x}\cosh\left(\frac{2\eta_{x}}{\alpha}\right) + 4\rho_{x}^{2}} , \quad x^{1} = \frac{4\alpha\rho_{x}^{2} - \alpha^{3}}{\alpha^{2} + 4\alpha\rho_{x}\cosh\left(\frac{2\eta_{x}}{\alpha}\right) + 4\rho_{x}^{2}}, \tag{56}$$

$$x^{0} = \frac{4\alpha^{2}\rho_{x}\sinh\left(\frac{2\eta_{x}}{\alpha}\right)}{\alpha^{2} + 4\alpha\rho_{x}\cosh\left(\frac{2\eta_{x}}{\alpha}\right) + 4\rho_{x}^{2}} , \quad x^{1} = \frac{4\alpha\rho_{x}^{2} - \alpha^{3}}{\alpha^{2} + 4\alpha\rho_{x}\cosh\left(\frac{2\eta_{x}}{\alpha}\right) + 4\rho_{x}^{2}}, \quad (56)$$

$$y^{0} = \frac{4\alpha^{2}\rho_{y}\sinh\left(\frac{2\eta_{y}}{\alpha}\right)}{\alpha^{2} + 4\alpha\rho_{y}\cosh\left(\frac{2\eta_{y}}{\alpha}\right) + 4\rho_{y}^{2}} , \quad y^{1} = \frac{4\alpha\rho_{y}^{2} - \alpha^{3}}{\alpha^{2} + 4\alpha\rho_{y}\cosh\left(\frac{2\eta_{y}}{\alpha}\right) + 4\rho_{y}^{2}}, \quad (57)$$

$$\bar{x}^{0} = \frac{4\alpha^{2}\bar{\rho}_{x}\sinh\left(\frac{2\bar{\eta}_{x}}{\alpha}\right)}{\alpha^{2} + 4\alpha\bar{\rho}_{x}\cosh\left(\frac{2\bar{\eta}_{x}}{\alpha}\right) + 4\bar{\rho}_{x}^{2}} , \quad \bar{x}^{1} = \frac{4\alpha\bar{\rho}_{x}^{2} - \alpha^{3}}{\alpha^{2} + 4\alpha\bar{\rho}_{x}\cosh\left(\frac{2\bar{\eta}_{x}}{\alpha}\right) + 4\bar{\rho}_{x}^{2}}, \quad (58)$$

$$\bar{y}^{0} = \frac{4\alpha^{2}\bar{\rho}_{y}\sinh\left(\frac{2\bar{\eta}_{y}}{\alpha}\right)}{\alpha^{2} + 4\alpha\bar{\rho}_{y}\cosh\left(\frac{2\bar{\eta}_{y}}{\alpha}\right) + 4\bar{\rho}_{y}^{2}} , \quad \bar{y}^{1} = \frac{4\alpha\bar{\rho}_{y}^{2} - \alpha^{3}}{\alpha^{2} + 4\alpha\bar{\rho}_{y}\cosh\left(\frac{2\bar{\eta}_{y}}{\alpha}\right) + 4\bar{\rho}_{y}^{2}}.$$
 (59)

Thus, we obtain the following squared spacetime intervals:

Path 1: 
$$\sigma^{2}(x,y) = -(x^{0} - y^{0})^{2} + (x^{1} - y^{1})^{2}$$

$$= \frac{16\alpha^{4} \left[\rho_{x}^{2} + \rho_{y}^{2} - 2\rho_{x}\rho_{y}\cosh\left(\frac{2(\eta_{y} - \eta_{x})}{\alpha}\right)\right]}{\left[\alpha^{2} + 4\alpha\rho_{x}\cosh\left(\frac{2\eta_{x}}{\alpha}\right) + 4\rho_{x}^{2}\right]\left[\alpha^{2} + 4\alpha\rho_{y}\cosh\left(\frac{2\eta_{y}}{\alpha}\right) + 4\rho_{y}^{2}\right]}, (60)$$

Path 2: 
$$\sigma^{2}(\bar{x}, \bar{y}) = -(\bar{y}^{0} - \bar{x}^{0})^{2} + (\bar{y}^{1} - \bar{x}^{1})^{2}$$

$$= \frac{16\alpha^{4} \left[\bar{\rho}_{x}^{2} + \bar{\rho}_{y}^{2} - 2\bar{\rho}_{x}\bar{\rho}_{y}\cosh\left(\frac{2(\bar{\eta}_{y} - \bar{\eta}_{x})}{\alpha}\right)\right]}{\left[\alpha^{2} + 4\alpha\bar{\rho}_{x}\cosh\left(\frac{2\bar{\eta}_{x}}{\alpha}\right) + 4\bar{\rho}_{x}^{2}\right] \left[\alpha^{2} + 4\alpha\bar{\rho}_{y}\cosh\left(\frac{2\bar{\eta}_{y}}{\alpha}\right) + 4\bar{\rho}_{y}^{2}\right]}.$$
 (61)

As anticipated, due to the explicit  $\eta$ -dependence of the causal diamond metric, the time dependence in Eqs. (60) and (61) arises not only through the intervals  $\Delta \eta = \eta_y - \eta_x$  and  $\Delta \bar{\eta} = \bar{\eta}_y - \bar{\eta}_x$ , but also through the individual coordinates  $\eta_{x,y}$  and  $\bar{\eta}_{x,y}$  appearing in the denominators. Consequently, we carry out the analysis within the near-horizon approximation, where, to leading order in the expansions given by Eqs. (18) and (19) for  $\rho \ll 1$ , and Eqs. (22) and (23) for  $\rho \gg 1$ , the spacetime geometry is effectively described by a static metric:

#### (1) For $\rho \ll 1$ :

Path 1: 
$$\sigma^{2}(x,y) = -(x^{0} - y^{0})^{2} + (x^{1} - y^{1})^{2}$$
  

$$= 16\rho_{x}^{2} + 16\rho_{y}^{2} - 32\rho_{x}\rho_{y}\cosh\left[\frac{2(\eta_{x} - \eta_{y})}{\alpha}\right] + \mathcal{O}(\rho_{x}^{3}, \rho_{y}^{3}), \qquad (62)$$

Path 2: 
$$\sigma^{2}(\bar{x}, \bar{y}) = -(\bar{y}^{0} - \bar{x}^{0})^{2} + (\bar{y}^{1} - \bar{x}^{1})^{2}$$
  

$$= 16\bar{\rho}_{x}^{2} + 16\bar{\rho}_{y}^{2} - 32\bar{\rho}_{x}\bar{\rho}_{y}\cosh\left[\frac{2(\bar{\eta}_{x} - \bar{\eta}_{y})}{\alpha}\right] + \mathcal{O}(\bar{\rho}_{x}^{3}, \bar{\rho}_{y}^{3}). \tag{63}$$

(2) For  $\rho \gg 1$ , or equivalently  $\tilde{\rho} \ll 1$ , by means of  $4\tilde{\rho} = \alpha^2/\rho$ :

Path 1: 
$$\sigma^{2}(x,y) = -(x^{0} - y^{0})^{2} + (x^{1} - y^{1})^{2}$$
  

$$= \frac{\alpha^{4}}{\rho_{x}^{2}} + \frac{\alpha^{4}}{\rho_{y}^{2}} - \frac{2\alpha^{4}}{\rho_{x}\rho_{y}} \cosh\left[\frac{2(\eta_{x} - \eta_{y})}{\alpha}\right] + \mathcal{O}(\rho_{x}^{-3}, \rho_{y}^{-3}), \tag{64}$$

$$=16\tilde{\rho}_x^2 + 16\tilde{\rho}_y^2 - 32\tilde{\rho}_x\tilde{\rho}_y \cosh\left[\frac{2(\eta_x - \eta_y)}{\alpha}\right] + \mathcal{O}(\tilde{\rho}_x^3, \tilde{\rho}_y^3), \tag{65}$$

Path 2: 
$$\sigma^{2}(\bar{x}, \bar{y}) = -(\bar{y}^{0} - \bar{x}^{0})^{2} + (\bar{y}^{1} - \bar{x}^{1})^{2}$$
  

$$= \frac{\alpha^{4}}{\bar{\rho}_{x}^{2}} + \frac{\alpha^{4}}{\bar{\rho}_{y}^{2}} - \frac{2\alpha^{4}}{\bar{\rho}_{x}\bar{\rho}_{y}} \cosh\left[\frac{2(\bar{\eta}_{x} - \bar{\eta}_{y})}{\alpha}\right] + \mathcal{O}(\bar{\rho}_{x}^{-3}, \bar{\rho}_{y}^{-3}), \tag{66}$$

$$=16\tilde{\rho}_x^2 + 16\tilde{\rho}_y^2 - 32\tilde{\rho}_x\tilde{\rho}_y \cosh\left[\frac{2(\eta_x - \eta_y)}{\alpha}\right] + \mathcal{O}(\tilde{\rho}_x^3, \tilde{\rho}_y^3). \tag{67}$$

In both cases  $\rho \ll 1$  and  $\rho \gg 1$  (where the geometry can be expressed in terms of  $\tilde{\rho} \ll 1$ ), the expressions reduce to the same form as in the analogous Rindler case, given in Eqs. (34) and (35), up to an overall factor of 16. Therefore, taking  $x^{\mu} = \bar{x}^{\mu}$  and  $\bar{y}^{\mu} = (-y^0, y^1)$ , as illustrated in Fig. 9c, leads to the same analysis performed in the Rindler case, as shown in Eqs. (36) and (37). The propagations along Path 1 and Path 2 are thus physically equivalent, which is fully consistent with the perspective of an inertial observer in Minkowski spacetime.

### 2. Propagation from the region $D_P$ to $D_R$ , and from $D_R$ to $D_F$

We now proceed directly with the configuration shown in Fig. 10a, where Path 1 corresponds to the propagation from the event  $y^{\mu} \equiv (y^0, y^1) \in D_P$  to  $x^{\mu} \equiv (x^0, x^1) \in D_R$ , and Path 2 corresponds to the propagation from  $x^{\mu} \equiv (x^0, x^1) \in D_R$  to  $\bar{y}^{\mu} \equiv (\bar{y}^0, \bar{y}^1) \in D_F$ , where we impose the identifications  $\bar{y}^0 = -y^0$  and  $\bar{y}^1 = y^1$ . In this way, we note that the calculation of the squared spacetime interval requires only the coordinate transformations given by Eqs. (9) and (17):

$$x^{0} = \frac{4\alpha^{2}\rho_{r}\sinh\left(\frac{2\eta_{r}}{\alpha}\right)}{\alpha^{2} + 4\alpha\rho_{r}\cosh\left(\frac{2\eta_{r}}{\alpha}\right) + 4\rho_{r}^{2}} , \quad x^{1} = \frac{-4\alpha\rho_{f}^{2} - \alpha^{3}}{\alpha^{2} + 4\alpha\rho_{f}\sinh\left(\frac{2\eta_{f}}{\alpha}\right) - 4\rho_{f}^{2}}, \quad (68)$$

$$y^{0} = \frac{-4\alpha^{2}\rho_{p}\cosh\left(\frac{2\eta_{p}}{\alpha}\right)}{\alpha^{2} - 4\alpha\rho_{p}\sinh\left(\frac{2\eta_{p}}{\alpha}\right) - 4\rho_{p}^{2}} , \quad y^{1} = \frac{-4\alpha\rho_{p}^{2} - \alpha^{3}}{\alpha^{2} - 4\alpha\rho_{p}\sinh\left(\frac{2\eta_{p}}{\alpha}\right) - 4\rho_{p}^{2}}.$$
 (69)

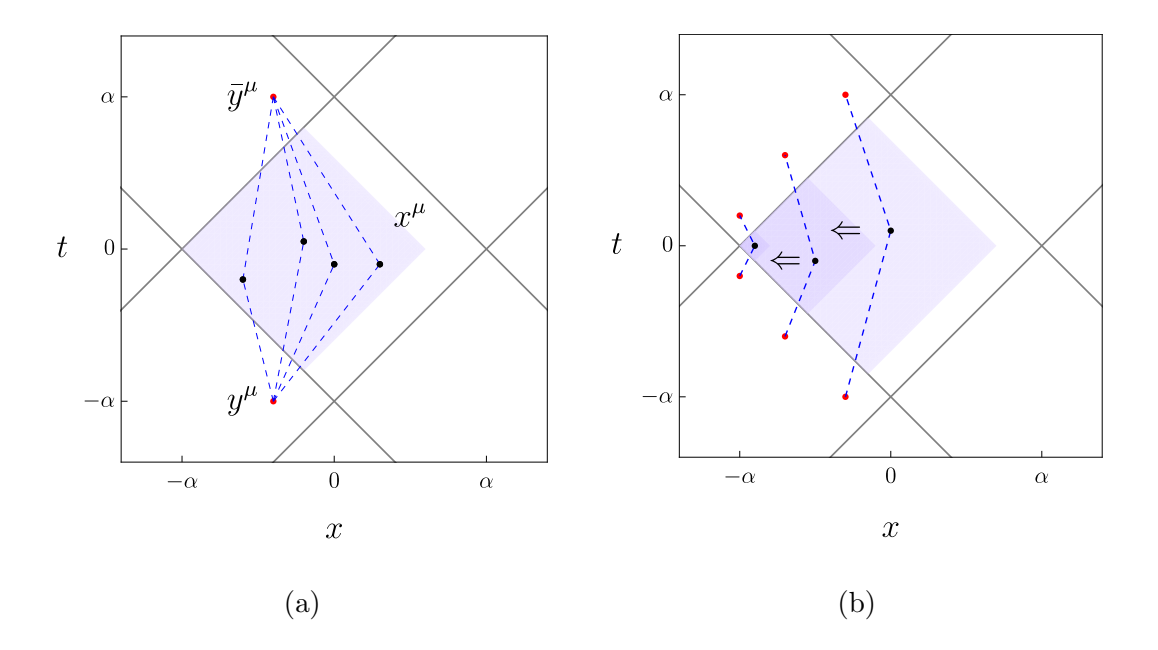


FIG. 10: (a) Paths 1 and 2, where  $x^{\mu} = \bar{x}^{\mu}$  and  $y^{\mu}$  is related to  $\bar{y}^{\mu}$  by a time reflection. (b) Near-horizon approximation.

Thus, we obtain the following squared spacetime intervals:

Path 1: 
$$\sigma^{2}(x,y) = -(x^{0} - y^{0})^{2} + (x^{1} - y^{1})^{2}$$

$$= \frac{16\alpha^{4} \left(-2\rho_{p}\rho_{r} \sinh\left(\frac{2(\eta_{r} - \eta_{p})}{\alpha}\right) - \rho_{p}^{2} + \rho_{r}^{2}\right)}{\left(\alpha^{2} - 4\alpha\rho_{p} \sinh\left(\frac{2\eta_{p}}{\alpha}\right) - 4\rho_{p}^{2}\right)\left(\alpha^{2} + 4\alpha\rho_{r} \cosh\left(\frac{2\eta_{r}}{\alpha}\right) + 4\rho_{r}^{2}\right)},$$
(70)
Path 2:  $\sigma^{2}(x,\bar{y}) = -(\bar{y}^{0} - x^{0})^{2} + (\bar{y}^{1} - x^{1})^{2}$ 

$$= \frac{16\alpha^{4} \left(2\rho_{p}\rho_{r} \sinh\left(\frac{2(\eta_{r} + \eta_{p})}{\alpha}\right) - \rho_{p}^{2} + \rho_{r}^{2}\right)}{\left(\alpha^{2} - 4\alpha\rho_{p} \sinh\left(\frac{2\eta_{p}}{\alpha}\right) - 4\rho_{p}^{2}\right)\left(\alpha^{2} + 4\alpha\rho_{r} \cosh\left(\frac{2\eta_{r}}{\alpha}\right) + 4\rho_{r}^{2}\right)}.$$
(71)

As seen in Eqs. (70) and (71), the dependence on  $\eta_{r,p}$  is intricate. However, the analysis can be simplified by considering the near-horizon approximation, where the spacetime geometry becomes effectively static. In this configuration (see Fig. 10b), the boundaries between  $D_P$  and  $D_R$ , and between  $D_R$  and  $D_F$ , correspond to the left past horizon  $\mathcal{H}_0^-$  and the left future horizon  $\mathcal{H}_0^+$ , respectively. By approaching these boundaries via the approximations  $\rho_{r,p,f} \ll 1$ , as illustrated in Fig. 3a, we obtain:

Path 1: 
$$\sigma^{2}(x,y) = -(x^{0} - y^{0})^{2} + (x^{1} - y^{1})^{2}$$
  
 $= 16\rho_{r}^{2} - 16\rho_{p}^{2} - 32\rho_{p}\rho_{r}\sinh\left[\frac{2(\eta_{r} - \eta_{p})}{\alpha}\right] + \mathcal{O}(\rho^{3})$   
 $\approx -32\rho_{p}\rho_{r}\sinh\left[\frac{2(\eta_{r} - \eta_{p})}{\alpha}\right],$  (72)  
Path 2:  $\sigma^{2}(x,\bar{y}) = -(\bar{y}^{0} - x^{0})^{2} + (\bar{y}^{1} - x^{1})^{2}$   
 $= 16\rho_{r}^{2} - 16\rho_{p}^{2} + 32\rho_{p}\rho_{r}\sinh\left[\frac{2(\eta_{r} + \eta_{p})}{\alpha}\right] + \mathcal{O}(\rho^{3})$   
 $\approx 32\rho_{p}\rho_{r}\sinh\left[\frac{2(\eta_{r} + \eta_{p})}{\alpha}\right],$  (73)

where we have assumed, without loss of generality within the present approximation, that  $16\rho_r^2 - 16\rho_p^2 \approx 0$ . As in the Rindler case, the squared spacetime intervals in this approximation capture the physical distinction between the processes associated with Paths 1 and 2; in particular, the emergence again of sinh instead of cosh in Eqs. (64)-(67).

Moreover, since the geometry is effectively static in the near-horizon approximation, the time dependence of the Feynman propagator is entirely encoded in the temporal intervals  $\Delta \eta = \eta_r - \eta_p$  and  $\Delta \bar{\eta} = \eta_r - \eta_f = \eta_r + \eta_p$ , where, similar to the Rindler case, one readily verifies that  $\eta_f = -\eta_p$ . Consequently, the Fourier transforms of  $G_F$  with respect to  $\Delta \eta$  and  $\Delta \bar{\eta}$  are effectively performed in terms of  $\eta_r$ .

The frequency-space propagator in the near-horizon approximation for Path 1 is given by

$$\tilde{G}_{F}^{\text{Path 1}}(\Omega, \rho_{p}, \rho_{r}) = \int_{-\infty}^{\infty} d\eta_{r} G_{F}^{\text{Path 1}}(\eta_{r} - \eta_{p}, \rho_{p}, \rho_{r}) e^{-i\Omega\eta_{r}} 
= \int_{-\infty}^{\infty} d(\Delta\eta) G_{F}^{\text{Path 1}}(\Delta\eta, \rho_{p}, \rho_{r}) e^{-i\Omega\Delta\eta} e^{-i\Omega\eta_{p}} 
= \int_{-\infty}^{\infty} d(\Delta\eta) \left(\frac{1}{4\pi} \int_{0}^{\infty} \frac{ds}{s} e^{\left[\frac{i}{4s}\left(-32\rho_{p}\rho_{r}\sinh\left[\frac{2\Delta\eta}{\alpha}\right]\right) - ism^{2} - s\epsilon\right]}\right) e^{-i\Omega\Delta\eta} e^{-i\Omega\eta_{p}} 
= \int_{0}^{\infty} \frac{ds}{4\pi s} e^{-ism^{2} - s\epsilon} \int_{-\infty}^{\infty} d(\Delta\eta) e^{-\frac{8i}{s}\rho_{p}\rho_{r}\sinh\left[\frac{2\Delta\eta}{\alpha}\right]} e^{-i\Omega\Delta\eta} e^{-i\Omega\eta_{p}} 
= \int_{0}^{\infty} \frac{ds}{4\pi s} e^{-ism^{2} - s\epsilon} \left[\alpha e^{-i\Omega\eta_{p}} e^{-\frac{\pi\Omega\alpha}{4}} K_{-i\Omega\alpha/2} \left(-\frac{8\rho_{p}\rho_{r}}{s}\right)\right], \tag{74}$$

where we have used the identity given in Eq. (51), with the substitutions  $\zeta = -4\rho_p \rho_r/s$ ,  $\gamma = e^{2\Delta\eta/\alpha}$ , and  $\nu = -\Omega\alpha/2$ . Thus, we have:

$$\tilde{G}_F^{\text{Path 1}}(-\Omega, \rho_p, \rho_r) = e^{\pi\Omega\alpha/2} \,\tilde{G}_F^{\text{Path 1}}(\Omega, \rho_p, \rho_r). \tag{75}$$

Next, for Path 2, we obtain:

$$\tilde{G}_{F}^{\text{Path 2}}(\bar{\Omega}, \rho_{p}, \rho_{r}) = \int_{-\infty}^{\infty} d\eta_{r} G_{F}^{\text{Path 2}}(\eta_{r} + \eta_{p}, \rho_{p}, \rho_{r}) e^{-i\bar{\Omega}\eta_{r}}$$

$$= \int_{-\infty}^{\infty} d(\Delta\bar{\eta}) G_{F}^{\text{Path 2}}(\Delta\bar{\eta}, \rho_{p}, \rho_{r}) e^{-i\bar{\Omega}\Delta\bar{\eta}} e^{i\bar{\Omega}\eta_{p}}$$

$$= \int_{-\infty}^{\infty} d(\Delta\bar{\eta}) \left(\frac{1}{4\pi} \int_{0}^{\infty} \frac{ds}{s} e^{\left[\frac{i}{4s} \left(32\rho_{p}\rho_{r} \sinh\left[\frac{2\Delta\bar{\eta}}{\alpha}\right]\right) - ism^{2} - s\epsilon\right]}\right) e^{-i\bar{\Omega}\Delta\bar{\eta}} e^{i\bar{\Omega}\eta_{p}}$$

$$= \int_{0}^{\infty} \frac{ds}{4\pi s} e^{-ism^{2} - s\epsilon} \int_{-\infty}^{\infty} d(\Delta\bar{\eta}) e^{\frac{8i}{s}\rho_{p}\rho_{r} \sinh\left[\frac{2\Delta\bar{\eta}}{\alpha}\right]} e^{-i\bar{\Omega}\Delta\bar{\eta}} e^{i\bar{\Omega}\eta_{p}}$$

$$= \int_{0}^{\infty} \frac{ds}{4\pi s} e^{-ism^{2} - s\epsilon} \left[\alpha e^{i\bar{\Omega}\eta_{p}} e^{\frac{\pi\bar{\Omega}\alpha}{4}} K_{i\bar{\Omega}\alpha/2} \left(-\frac{8\rho_{p}\rho_{r}}{s}\right)\right], \tag{76}$$

where, once again, we have used the change  $\Delta \bar{\eta} \to -\Delta \bar{\eta}$ , and the identity given in Eq. (51), with the substitutions  $\zeta = -4\rho_p \rho_r / s$ ,  $\gamma = e^{2\Delta \bar{\eta}/\alpha}$ , and  $\nu = \bar{\Omega}\alpha/2$ .

Furthermore, from Eq. (74), identifying  $\bar{\Omega} = \Omega$ , we obtain the following relation:

$$\tilde{G}_F^{\text{Path 2}}(\Omega, \rho_p, \rho_r) = \tilde{G}_F^{\text{Path 1}}(-\Omega, \rho_p, \rho_r). \tag{77}$$

Hence, from Eq. (75) we obtain:

$$\left| \frac{\tilde{G}_F^{\text{Path 1}}(\Omega, \rho_p, \rho_r)}{\tilde{G}_F^{\text{Path 2}}(\Omega, \rho_p, \rho_r)} \right|^2 = e^{-\beta\Omega} \quad , \quad \beta = \pi\alpha.$$
 (78)

Remarkably, this ratio takes the form of a thermal state, characterized by a Boltzmann factor, from which the effective temperature is given by

$$T = \frac{1}{\pi \alpha}.\tag{79}$$

The temperature obtained through this method is consistent with previous findings based on the thermal time hypothesis, the open quantum system approach, the thermofield-double construction, and related frameworks [13–15, 17, 18].

Therefore, the propagation associated with Path 1 can be interpreted as the emission of scalar quanta from the past horizon  $\mathcal{H}_0^-$ , as seen from the perspective of the observer in  $D_R$ , while the propagation associated with Path 2 represents the absorption of these scalar quanta at the future horizon  $\mathcal{H}_0^+$ . Then, just as in the case of the Rindler frame, although propagation across causal horizons appears physically equivalent from the perspective of an

inertial observer, restricting the observation to an observer confined to the causal diamond  $D_R$  reveals the thermal nature of these horizons, a feature otherwise hidden in the inertial propagator. It is also worth mentioning that a similar analysis can be carried out near the right boundary of  $D_R$ , by noting that  $\rho \gg 1$  can be mapped to  $\tilde{\rho} \ll 1$ , making the entire treatment fully analogous.

#### IV. DISCUSSION

In this article, we introduced a method in which: (1) the Feynman propagator was employed to detect the inequivalence of physical processes across causal horizons from the perspective of observers constrained to regions that are causally disconnected from the rest of Minkowski spacetime; (2) we implemented the Fourier transform following the convention used in the analysis of vacuum fluctuations; (3) we employed a specific setup involving the triad of events  $x^{\mu}$ ,  $y^{\mu}$ , and  $\bar{y}^{\mu}$ , where  $y^{0} < x^{0} < \bar{y}^{0}$ . Moreover,  $y^{\mu}$  and  $\bar{y}^{\mu}$  are related by a reflection in the Minkowski time coordinate. This setup enabled us to compute the ratio of propagators across the past and future horizons in the frequency domain.

Following this method, we showed that the Feynman propagator between events separated by the causal horizons of the right Rindler wedge R reveals that propagation across the past horizon, from the perspective of the Rindler observer, is naturally and causally interpreted as the emission of scalar quanta from the past horizon. Similarly, for the same observer, propagation across the future horizon is likewise interpreted as the absorption of scalar quanta at the future horizon. These results are fully consistent with the direction of time evolution inside the wedge R, due to the appropriate definition of the Fourier transform. Moreover, owing to the setup implemented between the events in the wedges P, R, and F, the ratio between emission and absorption processes at the past and future horizons, respectively, gives rise to a Boltzmann factor with a temperature precisely matching that predicted by the Unruh effect.

Finally, we extended this treatment to the causal diamond region  $D_R$ . Since the implemented method imposes no constraints on the relative distance of events from the causal horizon, we were able, without loss of generality, to apply the near-horizon approximation

where the effective geometry becomes static. This approximation significantly simplified the calculation and yielded a consistent Fourier transform in the interval  $\Delta \eta$ . In this fashion, we recovered, qualitatively, the same results as in the analysis of the right Rindler wedge R. These findings demonstrate that thermality in quantum field theory can emerge directly from causal restrictions, suggesting that causal diamonds, as minimal units of causal structure, encode fundamental thermodynamic behavior without invoking accelerated frames or gravitational backgrounds. This perspective offers a promising framework for exploring the interplay of quantum fields, causal geometry, and emergent spacetime thermodynamics.

#### ACKNOWLEDGMENTS

We would like to thank the attendees of the 2025 TAMU-Princeton-Caspar-Baylor-CSU-UIUC Summer School, where these and other results were first presented, for their interest and many questions. We are especially grateful to Wolfgang Schleich for his careful reading of a draft version of the paper, for his thoughtful questions and suggestions and for his encouragement to publish these results. All the authors of this paper were partially supported by the Army Research Office (ARO) under Grant No. W911NF-23-1-0202. In addition, G.V.-M. gratefully acknowledges the Center for Mexican American and Latino/a Studies at the University of Houston for their generous support through a Lydia Mendoza Fellowship.

<sup>[1]</sup> T. Padmanabhan, Thermality of the rindler horizon: A simple derivation from the structure of the inertial propagator, Physical Review D **100**, 045024 (2019).

<sup>[2]</sup> S. A. Fulling, Nonuniqueness of canonical field quantization in riemannian space-time, Physical Review D 7, 2850 (1973).

<sup>[3]</sup> P. C. Davies, Scalar production in schwarzschild and rindler metrics, Journal of Physics A: Mathematical and General 8, 609 (1975).

<sup>[4]</sup> W. G. Unruh, Notes on black-hole evaporation, Physical Review D 14, 870 (1976).

<sup>[5]</sup> N. D. Birrell and P. C. W. Davies, *Quantum fields in curved space* (Cambridge university press, 1984).

<sup>[6]</sup> B. S. DeWitt, The global approach to quantum field theory. Vol. 1, 2, Vol. 114 (2003).

- [7] S. Weinberg, The quantum theory of fields. Volume 1: foundations (1995).
- [8] M. Srednicki, Quantum field theory (Cambridge university press, 2007).
- [9] T. Padmanabhan, Quantum Field Theory: The Why, What and How (Springer, 2016).
- [10] H. Camblong, A. Chakraborty, P. Lopez-Duque, and C. Ordóñez, Entanglement degradation in causal diamonds, Physical Review D 109, 105003 (2024).
- [11] P. Francesco, P. Mathieu, and D. Sénéchal, *Conformal field theory* (Springer Science & Business Media, 2012).
- [12] I. S. Gradshteyn and I. M. Ryzhik, *Table of integrals, series, and products* (Academic press, 2014).
- [13] H. Camblong, A. Chakraborty, P. Lopez-Duque, and C. Ordóñez, Conformal quantum mechanics of causal diamonds: Time evolution, thermality, and instability via path integral functionals, Physical Review D 110, 124043 (2024).
- [14] A. Chakraborty, C. R. Ordóñez, and G. Valdivia-Mera, Path integral derivation of the thermofield double state in causal diamonds, Classical and Quantum Gravity 42, 025015 (2024).
- [15] M. Arzano, Conformal quantum mechanics of causal diamonds, Journal of High Energy Physics **2020**, 1 (2020).
- [16] H. Camblong, A. Chakraborty, P. Lopez Duque, and C. Ordóñez, Spectral properties of the symmetry generators of conformal quantum mechanics: a path-integral approach, Journal of Mathematical Physics 64, 092302 (2023).
- [17] P. Martinetti and C. Rovelli, Diamond's temperature: Unruh effect for bounded trajectories and thermal time hypothesis, Classical and Quantum Gravity **20**, 4919 (2003).
- [18] A. Chakraborty, H. Camblong, and C. Ordóñez, Thermal effect in a causal diamond: Open quantum systems approach, Physical Review D **106**, 045027 (2022).